

# A LEAST SQUARES RADIAL BASIS FUNCTION FINITE DIFFERENCE METHOD WITH IMPROVED STABILITY PROPERTIES

IGOR TOMINEC\*, ELISABETH LARSSON\*, AND ALFA HERYUDONO†

**Abstract.** Localized collocation methods based on radial basis functions (RBFs) for elliptic problems appear to be non-robust in the presence of Neumann boundary conditions. In this paper we overcome this issue by formulating the RBF-generated finite difference method in a discrete least-squares setting instead. This allows us to prove high-order convergence under node refinement and to numerically verify that the least-squares formulation is more accurate and robust than the collocation formulation. The implementation effort for the modified algorithm is comparable to that for the collocation method.

**Key words.** radial basis function, least-squares, partial differential equation, elliptic problem, Neumann condition, RBF-FD

**AMS subject classifications.** 65N06, 65N12, 65N35

**1. Introduction.** Radial basis function-generated finite difference methods (RBF-FD) generalize classical finite difference methods (FD) to scattered node settings. However, while FD uses tensor products of one-dimensional derivative approximations, RBF-FD directly computes multivariate approximations, which is an advantage when differentiation is not aligned with a coordinate direction [14]. In this paper, we generalize RBF-FD to a least squares setting (RBF-FD-LS), which improves stability and accuracy.

RBF-FD is a meshfree method, which provides flexibility with respect to the geometry. In contrast to FD methods where an entire coordinate dimension is affected by adaptive refinement, RBF-FD allows for coordinate independent local adaptivity [18].

The RBF-FD method was first introduced by Tolstykh in 2000 [28], and other early papers include [26, 30]. The method is based on the idea that given scattered nodes  $x_j \in \mathbb{R}^d$ ,  $j = 1, \dots, n$ , in the neighborhood of a point  $x$ , we can create a localized RBF approximation of the function  $u(x)$  using these 'stencil points',

$$(1.1) \quad u_h(x) = \sum_{j=1}^n c_j \phi(\|x - x_j\|) \equiv \sum_{j=1}^n c_j \phi_j(x),$$

where  $h$  is a measure of the inter-nodal distance,  $\phi(r)$  is a radial basis function, and  $c_j$  are unknown coefficients. The interpolation conditions  $u_h(x_i) = u(x_i)$  lead to the linear system

$$(1.2) \quad \underbrace{\begin{pmatrix} \phi_1(x_1) & \cdots & \phi_n(x_1) \\ \vdots & & \vdots \\ \phi_1(x_n) & \cdots & \phi_n(x_n) \end{pmatrix}}_A \begin{pmatrix} c_1 \\ \vdots \\ c_n \end{pmatrix} = \begin{pmatrix} u(x_1) \\ \vdots \\ u(x_n) \end{pmatrix}$$

\*Uppsala University, Department of Information Technology, SE-751 05 Uppsala, Sweden (igor.tominec@it.uu.se, elisabeth.larsson@it.uu.se).

†University of Massachusetts Dartmouth, Department of Mathematics, Dartmouth, MA 02747, USA (aheryudono@umassd.edu).

**Funding:** The work of the first and the second author was supported by the Swedish Research Council, grant no. 2016-04849. The third author thanks University of Massachusetts Dartmouth for financially supporting his sabbatical leave and Department of Information Technology, Uppsala University, for hosting his sabbatical visit in Spring 2019.

If we let  $\underline{c} = (c_1, \dots, c_n)^T$  and  $\underline{u} = (u(x_1), \dots, u(x_n))^T$ , we have that  $\underline{c} = A^{-1}\underline{u}$ . A benefit of using RBFs is that for commonly used radial functions  $\phi(r)$  the matrix  $A$  is guaranteed to be non-singular for distinct node points [23, 17]. We can then proceed to apply an operator to the approximation:

$$(1.3) \quad \begin{aligned} \mathcal{L}u_h(x) &= \sum_{j=1}^n c_j \mathcal{L}\phi_j(x) \\ &= \underbrace{(\mathcal{L}\phi_1(x), \dots, \mathcal{L}\phi_n(x))}_{a^{\mathcal{L}}} \underline{c} = a^{\mathcal{L}} A^{-1} \underline{u} \equiv (\mathcal{L}\psi_1(x), \dots, \mathcal{L}\psi_n(x)) \underline{u} \equiv w^{\mathcal{L}} \underline{u}, \end{aligned}$$

where  $\{\psi_j(x)\}_{j=1}^n$ , forms a cardinal basis for the local interpolant, i.e.,  $\psi_j(x_i) = \delta_{ij}$ , and  $w^{\mathcal{L}}$  are the stencil weights used for approximating the operator at the point  $x$ .

In the early work on RBF-FD, infinitely smooth RBFs as the Gaussian RBF with  $\phi(r) = \exp(-r^2)$  or the multiquadric RBF with  $\phi(r) = \sqrt{1+r^2}$  were used. Lately, there has been an increasing interest in using piecewise smooth polyharmonic splines (PHS) with  $\phi(r) = |r|^{2k-1}$ ,  $k \geq 1$ . These are conditionally positive definite functions. It was shown in [17] that by adding a polynomial basis of a degree corresponding to the order of conditional positive definiteness and constraining the RBF coefficients  $\underline{c}$  to be orthogonal to this basis, we can guarantee strict positive definiteness of the quadratic form  $\underline{c}^T A \underline{c}$ , which is important when proving optimality results. The RBF approximation then takes the form

$$(1.4) \quad u_h(x) = \sum_{j=1}^n c_j \phi_j(x) + \sum_{j=1}^m \beta_j p_j(x), \quad \sum_{j=1}^n c_j p_k(x_j) = 0.$$

where the second equation is the constraint. The dimension  $m$  of the polynomial space is given by the degree  $p$  of the polynomial as  $m = \binom{p+d}{d}$ , where  $d$  is the number of spatial dimensions. In the PhD thesis [2], and the subsequent papers [11, 12, 5, 4] it was shown that it is beneficial to append a polynomial of a higher degree  $p$  than strictly required. First, the convergence order of the method depends on  $p$  [3]. Secondly, the behavior near boundaries is improved compared with classical polynomial-based FD [4]. It was suggested in [12] that for a two-dimensional problem, using a stencil size  $n = 2m$ , leads to a robust method. We use this strategy in this paper.

The interpolation relation corresponding to (1.2) for the polynomially augmented case becomes

$$(1.5) \quad \underbrace{\begin{pmatrix} A & P \\ P^T & 0 \end{pmatrix}}_{\tilde{A}} \begin{pmatrix} \underline{c} \\ \underline{\beta} \end{pmatrix} = \begin{pmatrix} \underline{u} \\ 0 \end{pmatrix},$$

where  $P_{ij} = p_j(x_i)$ , and  $\underline{\beta} = (\beta_1, \dots, \beta_m)^T$ . Similarly to (1.3), using (1.5) for the coefficient vectors, we get the differentiation relation

$$(1.6) \quad \begin{aligned} \mathcal{L}u_h(x) &= \underbrace{(a^{\mathcal{L}} \quad p^{\mathcal{L}})}_{b^{\mathcal{L}}} \begin{pmatrix} \underline{c} \\ \underline{\beta} \end{pmatrix} \\ &= b^{\mathcal{L}} \tilde{A}^{-1} \begin{pmatrix} \underline{u} \\ 0 \end{pmatrix} = (b^{\mathcal{L}} \tilde{A}^{-1})_{1:n} \underline{u} \equiv (\mathcal{L}\psi_1(x) \cdots \mathcal{L}\psi_n(x)) \underline{u} \equiv w^{\mathcal{L}} \underline{u}, \end{aligned}$$

where  $p^{\mathcal{L}} = (\mathcal{L}p_1(x), \dots, \mathcal{L}p_m(x))$ . The PHS + polynomial RBF-FD method works well, but there is some sensitivity to the node layout, e.g,  $P$  can become rank deficient for Cartesian node layouts. Several authors have developed algorithms for high

quality scattered node generation [13, 25, 27, 29]. Another issue that we have encountered, and that was also noted in [16] is that errors become large at boundaries with Neumann boundary conditions.

In this paper, we propose to improve the performance of the PHS + polynomial RBF-FD method by introducing least squares approximation (oversampling) at the PDE level. The least squares approach is also applicable to RBF-FD with other types of basis functions. A related study is [15], where least squares approximation is introduced in a RBF partition of unity method (RBF-PUM). It was shown that least squares RBF-PUM is numerically stable under patch refinement, which is not the case for collocation RBF-PUM. In [22] it is shown under quite general conditions that given enough oversampling, a wide class of discretizations are uniformly stable.

A recent paper [10] analyses a least-squares RBF-FD method formulated over a closed manifold. The formulation of the method is different from ours in that node points and evaluation points are the same, the oversampling is determined by the stencil size, and the theoretical analysis is performed using other strategies. Least squares approximation has been used together with RBF-FD by other authors to address some specific problems. In [16], an over-determined linear system is formed by enforcing both the PDE and the Dirichlet boundary conditions on the boundary, to improve the stability of the method. In [20] the context is the closest point method applied to a problem with a moving boundary in combination with RBF-FD. Enforcement of both the PDE and the constant-along-a-normal property of the closest point solution leads to an over-determined system and a robust method.

The main contributions of this paper are

- The RBF-FD-LS algorithm, which performs better than collocation-based RBF-FD in terms of efficiency, and stability for the tested PDE problems.
- Error estimates for RBF-FD-LS approximations when using the PHS + polynomial basis that have been validated numerically.
- A better understanding of the properties of RBF-FD approximations in terms of a piecewise continuous trial space.

The outline of this paper is as follows: In [section 2](#), we define a Poisson problem with Dirichlet and Neumann boundary conditions. Then in [section 3](#), we derive the RBF-FD-LS method. [section 4](#) focuses on the properties of the RBF-FD trial space, and then convergence and error estimates are derived in [section 5](#). Numerical experiments that validate the theoretical results are shown in [section 6](#). The paper ends with final remarks on the method and results in [section 7](#).

**2. The model problem.** We build our understanding on a model problem, the Poisson equation with Dirichlet and Neumann boundary data:

$$(2.1) \quad \begin{aligned} \mathcal{L}_2 u(y) &\equiv \Delta u(y) = f_2(y), & y \in \Omega, \\ \mathcal{L}_0 u(y) &\equiv u(y) = f_0(y), & y \in \partial\Omega_0, \\ \mathcal{L}_1 u(y) &\equiv \nabla u(y) \cdot n = f_1(y), & y \in \partial\Omega_1. \end{aligned}$$

When working with the PDE problem it is practical to have a unified formulation. We reformulate the system above as

$$(2.2) \quad D(y)u(y) = F(y),$$

where the specific operator  $D(y) = \mathcal{L}_i$  and right hand side function  $F(y) = f_i(y)$  depend on the location of  $y$ .

The regularity of the problem depends on the geometry of the domain  $\Omega$  in combination with the given right hand side functions. In the problems that we solve in this

paper, the domain is either smooth or convex, and the data is chosen such that the solution has bounded and continuous second derivatives. This ensures that the PDE problem (2.1) is well-defined pointwise. In order to achieve higher order convergence, we require the solution to have additional smoothness. We define the  $L_2$ -norm over a domain  $\Omega$  as  $\|u\|_{L_2(\Omega)}^2 = \int_{\Omega} u(y)^2 dy$ , and use the notation  $\|u\|_{L_2(\Omega)} = \|u\|_{\Omega}$  for brevity. We require  $u \in W_2^{p+1}(\Omega) = \{u \mid \|D^{\alpha}u\|_{L_2(\Omega)} < \infty, |\alpha| \leq p+1\}$ , where  $p \geq 2$  is the degree of the polynomial basis added to the PHS approximation (1.4) that we use in the numerical method.

Since we solve the discretized problem in the least squares sense, it is convenient for the theoretical results derived in section 5 to state also the continuous problem in least squares form. We require  $\tilde{u} \in V \subset W_2^{p+1}(\Omega)$  for the least squares solution. The squared  $L_2$ -norm of the residual of the PDE problem for a function  $v \in V$  is given by

$$\begin{aligned} \|r(v)\|_{L_2(\Omega)}^2 &= \int_{\partial\Omega_0} (\mathcal{L}_0 v(y) - f_0(y))^2 + \int_{\partial\Omega_1} (L_1 v(y) - f_1(y))^2 + \int_{\Omega} (\mathcal{L}_2 v(y) - f_2(y))^2 \\ (2.3) \quad &= \int_{\partial\Omega_0} (\mathcal{L}_0(v-u))^2 dy + \int_{\partial\Omega_1} (\mathcal{L}_1(v-u))^2 dy + \int_{\Omega} (\mathcal{L}_2(v-u))^2 dy, \end{aligned}$$

where  $f_i = L_i u$  was used in the second equality. If we introduce the bilinear form

$$(2.4) \quad a(u, v) = \int_{\partial\Omega_0} uv dy + \int_{\partial\Omega_1} \frac{\partial u}{\partial n} \frac{\partial v}{\partial n} dy + \int_{\Omega} \Delta u \Delta v dy,$$

and note that  $\|r(v)\|_{L_2(\Omega)}^2 = a(v-u, v-u)$ , the least squares solution of (2.1) is:

$$(2.5) \quad \tilde{u} = \arg \min_{v \in V} a(v-u, v-u).$$

Alternatively, using that the residual is  $a$ -orthogonal to  $V$ , we can write

$$(2.6) \quad a(\tilde{u} - u, v) = 0, \quad \forall v \in V.$$

When  $u \in V$ , the least squares problem solves the PDE problem exactly, but in general for a numerical approximation,  $u$  and  $\tilde{u}$  reside in different subspaces, leading to a non-zero residual.

**3. Formulation of RBF-FD-LS in practice.** We start with generating a node set  $X = \{x_k\}_{k=1}^N$  that covers the domain  $\Omega$ , on which we solve the PDE problem (2.2). It is beneficial for the approximation quality if the node distance is nearly uniform or varies smoothly over the domain. We associate each  $x_k$  with a stencil and denote the  $n$  points (including  $x_k$ ) in the local neighborhood of  $x_k$  that contribute to the stencil by  $X_k$ . An example of a global node set and a stencil is given in the left part of Figure 1.

To evaluate the RBF-FD approximation at a point  $y \in \bar{\Omega}$ , we need a stencil selection method. In our algorithm we choose the stencil associated with the point  $x_k$  that is closest to  $y$ . That is,

$$(3.1) \quad k(y) = \arg \min_i \|y - x_i\|.$$

A practical issue is that there are always points that are equally close to two or more stencils. Therefore we also need to break the tie, such that each  $y$  is uniquely

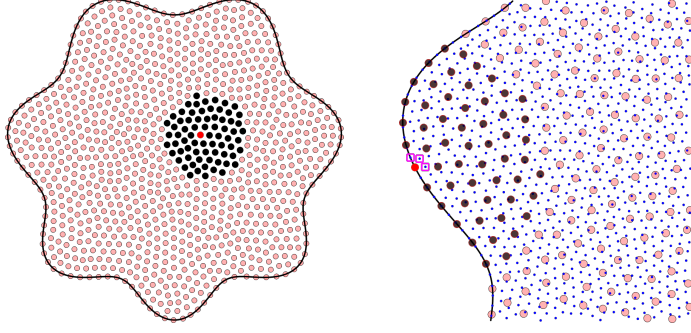


FIG. 1. The black curve represents the domain boundary  $\partial\Omega$ , the pale-red dots distributed over  $\Omega$  are the points in the node set  $X$ , the black dots are in each case the node points belonging to the stencil centered at the red point. The evaluation points in the node set  $Y$  are shown in the right subfigure as blue dots. It is also indicated with square markers which evaluation points select this particular stencil for evaluating  $u_h$ .

associated with one stencil. We then use (1.6) to write down the global RBF-FD approximation to the solution of the PDE problem evaluated at the point  $y$  as

$$(3.2) \quad u_h(y) = (b_k^{\mathcal{L}_0} \tilde{A}_k^{-1})_{1:n} u_h(X_k) = (\psi_1^k(y), \dots, \psi_n^k(y)) u_h(X_k) = w_k^{\mathcal{L}_0} u_h(X_k),$$

where the subscript or superscript  $k = k(y)$  indicates quantities computed in the stencil associated with  $x_k$ , and where  $u_h(X_k)$  is a column vector with  $u_h$  evaluated at the local node set. The expression for the action of a differential operator  $D(y)$  on the global RBF approximation  $u_h$ , evaluated at the point  $y$ , follows from (3.2):

$$(3.3) \quad D(y)u_h(y) = (D(y)\psi_1^k(y), \dots, D(y)\psi_n^k(y)) u_h(X_k) = w_k^{D(y)} u_h(X_k).$$

We note that the local matrices  $\tilde{A}_k$  can be reused for all points  $y$  that select the same stencil, and for all operators.

To solve the PDE problem (2.2), we sample the approximation (3.3) and the PDE data  $F(y)$  at a global node set  $Y = \{y_i\}_{i=1}^M$  that has to contain nodes in  $\Omega$ , at  $\partial\Omega_0$ , and at  $\partial\Omega_1$ . An example of an evaluation node set  $Y$  is shown in the right part of Figure 1. We construct a sparse global linear system

$$(3.4) \quad D_h(Y, X)u_h(X) = F(Y),$$

where row  $i$  contains the equation for  $D(y_i)u_h(y_i) = F(y_i)$  and the corresponding weights from (3.3) are entered into the columns corresponding to the global indices of the nodes in  $X_k$ . In the same way, we form the relation

$$(3.5) \quad u_h(Y) = E_h(Y, X)u_h(X),$$

using weights from (3.2). If the number of evaluation points  $M > N$ , both  $D_h(Y, X)$  and  $E_h(Y, X)$  are rectangular  $M \times N$  matrices.

In the discretized PDE problem,  $u_h(X)$  is the vector of unknowns, and we formally write the least squares solution of the linear system as

$$(3.6) \quad u_h(X) = D_h^+(Y, X) F(Y),$$

where the  $N \times M$  matrix  $D_h^+(Y, X) = (D_h^T D_h)^{-1} D_h^T$  is the pseudo inverse of  $D_h(Y, X)$ . To evaluate the solution at  $Y$  we add the step (3.5) to get

$$(3.7) \quad u_h(Y) = E_h(Y, X) D_h^+(Y, X) F(Y).$$

The over-determined linear system (3.4) can also be formulated as a discrete residual minimization problem. We define the residual

$$(3.8) \quad r(Y) = D_h(Y, X)u_h(X) - F(Y).$$

Then the solution (3.6) minimizes  $\|r(Y)\|_2^2$ , and it also holds that

$$(3.9) \quad D_h^T r(Y) = 0,$$

due to the orthogonality property of the least squares residual.

The collocation RBF-FD method, where  $Y = X$ , is a special case of the derivation above, where the stencil selected for  $y_k = x_k$  is always  $k$ ,  $D_h^+(X, X) = D_h^{-1}(X, X)$ , and  $E_h(X, X) = I_h$ . This leads to

$$(3.10) \quad r(X) = D_h(X, X)u_h(X) - F(X) = D_h(X, X)(D_h^{-1}(X, X)F(X)) - F(X) = \underline{0}.$$

In the discrete minimization of the residual (3.8), each equation has the same weight. This may cause problems with convergence to the PDE solution under node refinement. We start by introducing a weighted discrete  $\ell_2$ -norm that corresponds to the continuous  $L_2$ -norm with the integral replaced by a discrete quadrature formula. The error in this approximation is further discussed in subsection 5.4. We leave place holders  $\beta_i$  for additional balancing of the different parts of the residual, and discuss these further in subsection 5.5. Let a domain  $\Omega$  be discretized by  $M$  points  $y_i$ ,  $i = 1, \dots, M$ . Then

$$(3.11) \quad (u, v)_{\ell_2(\Omega)} = \frac{|\Omega|}{M} \sum_{i=1}^M u(y_i)v(y_i), \quad \|u\|_{\ell_2(\Omega)}^2 = (u, u)_{\ell_2(\Omega)},$$

where  $|\Omega| = \int_{\Omega} 1 dy$ . We denote the number of evaluation points that discretize the operator  $\mathcal{L}_i$  in (2.1) by  $M_i$  and note that if the evaluation points are quasi uniform with node distance  $h_y$ , then

$$(3.12) \quad h_y = c_0 \frac{|\partial\Omega_0|}{M_0} = c_1 \frac{|\partial\Omega_1|}{M_1} = c_2 \frac{\sqrt{|\Omega|}}{\sqrt{M_2}},$$

where  $c_0 \approx c_1 \approx c_2 \approx 1$ . Scaling the evaluation matrix as  $\bar{E}_h = \frac{\sqrt{|\Omega|}}{\sqrt{M}} E_h$  leads to

$$(3.13) \quad \|u_h\|_{\ell_2(\Omega)}^2 = \frac{|\Omega|}{M} \|u_h(Y)\|_2^2 = \|\bar{E}_h u_h(X)\|_2^2 = u_h(X)^T \bar{E}_h^T \bar{E}_h u_h(X).$$

For  $D_h$ , we scale according to the location of  $y$ , such that  $\bar{D}_h = \text{diag}(\beta(Y))D_h$ , where

$$(3.14) \quad \beta(y) = \begin{cases} \sqrt{\frac{|\partial\Omega_0|}{M_0}} \beta_0 & \approx \sqrt{h_y} \beta_0, & y \in \partial\Omega_0, \\ \sqrt{\frac{|\partial\Omega_1|}{M_1}} \beta_1 & \approx \sqrt{h_y} \beta_1, & y \in \partial\Omega_1, \\ \sqrt{\frac{|\Omega|}{M_2}} \beta_2 & \approx h_y \beta_2, & y \in \Omega, \end{cases}$$

and, similarly, we let  $\bar{F}(y) = \beta(y)F(y)$ . For the scaled residual  $\bar{r}(Y)$ , noting that  $D_h(Y, X)u_h(X) = D(Y)u_h(Y)$  and  $F(Y) = D(Y)u(Y)$ , we get

$$(3.15) \quad \begin{aligned} \|\bar{r}(Y)\|_2^2 &= \|\bar{D}_h(Y, X)u_h(X) - \bar{F}(Y)\|_2^2 = \|\beta(Y)D(Y)(u_h(Y) - u(Y))\|_2^2 \\ &= \beta_0^2 \|\mathcal{L}_0(u_h - u)\|_{\ell_2(\partial\Omega_0)}^2 + \beta_1^2 \|\mathcal{L}_1(u_h - u)\|_{\ell_2(\partial\Omega_1)}^2 + \beta_2^2 \|\mathcal{L}_2(u_h - u)\|_{\ell_2(\Omega)}^2. \end{aligned}$$

Comparing with the residual of the continuous problem (2.3) and the continuous bilinear form (2.4), we introduce the discrete bilinear form

$$(3.16) \quad a_h(u, v) = \beta_0^2 (u, v)_{\ell_2(\partial\Omega_0)} + \beta_1^2 \left( \frac{\partial u}{\partial n}, \frac{\partial v}{\partial n} \right)_{\ell_2(\partial\Omega_1)} + \beta_2^2 (\Delta u, \Delta v)_{\ell_2(\Omega)}.$$

So far, we have assumed that the Dirichlet boundary conditions are enforced in the least squares sense. It has been noted, e.g. in [21] that when Dirichlet conditions are imposed strongly, the overall accuracy is improved. Assuming that there are node points  $X_{\partial\Omega_0} \subset X$  that discretize the Dirichlet boundary, we let  $\tilde{X} = X \setminus X_{\partial\Omega_0}$  and  $u_h(X_{\partial\Omega_0}) = 0$ . Then we rewrite the discretized least squares PDE problem (3.4) as:

$$(3.17) \quad \bar{D}_h(Y, \tilde{X})u_h(\tilde{X}) = \bar{F}(Y) - \bar{D}_h(Y, X_{\partial\Omega_0})u_h^0(X_{\partial\Omega_0}) \equiv \tilde{F}(Y),$$

where  $u_h^0(X_{\partial\Omega_0}) = f_0(X_{\partial\Omega_0})$  is a subset of the Dirichlet boundary data. Note that  $u_h$  is in general non-zero at the Dirichlet boundary between the data points. The solution to the original problem is given by  $u_h + u_h^0 \in V_h$ . We denote the trial space with zero Dirichlet data by  $V_h^0$  and note that  $u_h \in V_h^0$ . Similarly to (2.5), we write the least squares problem on the form

$$(3.18) \quad u_h = \arg \min_{v_h \in V_h^0} a_h(v_h + u_h^0 - u, v_h + u_h^0 - u),$$

where  $V_h$  is the RBF-FD trial space. We have the orthogonality property

$$(3.19) \quad a_h(u_h + u_h^0 - u, v_h) = 0, \quad \forall v_h \in V_h^0.$$

To see how this relates to the matrix-based description of the discrete least squares problem, we introduce a (non-orthogonal) basis for  $V_h$ . For each evaluation point  $y$  there is a unique representation of  $u_h$  in terms of the local cardinal functions (3.2). We define global cardinal functions as

$$(3.20) \quad \Psi_j(y) = \begin{cases} \psi_i^k(y), & x_j \in X_k \\ 0, & x_j \notin X_k, \end{cases}$$

where  $k = k(y)$  is the stencil selected for the evaluation point  $y$ , and  $i(j)$  is the local index  $i$  in  $X_k$  of  $x_j \in X$ . We represent a non-homogeneous function  $u_h \in V_h$  as

$$(3.21) \quad u_h(y) = \sum_{j=1}^N u_h(x_j) \Psi_j(x).$$

We note that  $D_h(y_i, x_j) = D(y_i) \Psi_j(y_i)$  and  $E_h(y_i, x_j) = \Psi_j(y_i)$ . If we insert (3.21) in (3.19) and let  $v_h = \Psi_i$ , we get

$$(3.22) \quad \sum_{j=1}^N a_h(\Psi_j, \Psi_i) u_h(x_j) = a_h(u, \Psi_i),$$

where  $a_h(\Psi_j, \Psi_i)$  is an element of the matrix  $\bar{D}_h(Y, X)^T \bar{D}_h(Y, X)$ , and  $a_h(u, \Psi_i)$  is an element of the right hand side vector  $\bar{D}_h(Y, X)^T \bar{F}(Y)$  in the weighted normal equations. The specific properties of the trial space and the cardinal basis functions are further discussed in the following section.

**4. The discontinuous trial space.** The trial space  $V_h$  is a piecewise space. The stencil selection algorithm that we use for the evaluation points results in the domain being divided into Voronoi regions  $V_k$  around each stencil center point  $x_k \in X$ . Locally we have  $u_h \in W_2^2(V_k)$  due to the smoothness of the at least cubic PHS basis.

Scattered node sets are often quantified in terms of their fill distance  $h$ , which measures the radius of the largest ball empty of nodes in  $\Omega$ , and their separation distance  $s$ , defined by:

$$(4.1) \quad h = \sup_{x \in \Omega} \min_{x_j \in X} \|x - x_j\|_2 \geq s = \frac{1}{2} \min_{\substack{j \neq k \\ x_j, x_k \in X}} \|x_j - x_k\|_2,$$

For a quasi uniform node set  $s = c_s h \leq h$ , with  $c_s \lesssim 1$  locally and globally. Following [3], we can assess the interpolation error  $e_I = u_h - u$  at a point  $y$  in the Voronoi region  $V_k$  associated with  $x_k$  through Taylor expansion. We have that

$$(4.2) \quad |u_h(y) - u(y)| \leq \alpha_{k,0} h^{p+1} |u|_{W_\infty^{p+1}(V_k)},$$

where  $|u|_{W_\infty^q(\Omega)} = \sum_{|\alpha|=q} \|D^\alpha u\|_{L_\infty(\Omega)}$ , and the constant  $\alpha_{k,0}$  depends on the degree  $p$  of the polynomial basis, and on the node layout in the stencil. If the node layout is non-uniform, indicated by a small value of  $c_s$ , then the interpolation problem has a large Lebesgue constant [24], and consequently a larger interpolation error. The error is also larger for skewed stencils that are evaluated close to their support boundary.

If we apply an operator of order  $i$  to the interpolation error, we get the estimate

$$(4.3) \quad |\mathcal{L}_i(u_h(y) - u(y))| \leq \alpha_{k,i} h^{p+1-i} |u|_{W_\infty^{p+1}(V_k)}.$$

At the edge of a Voronoi region  $u_h$  takes slightly different values from each side. Let  $V_k$  and  $V_m$  have a common edge, and let  $y_{km}$  be a point on the edge. Then

$$(4.4) \quad |u_h(y_{km}^+) - u_h(y_{km}^-)| \leq (\alpha_{k,0} + \alpha_{m,0}) h^{p+1} |u|_{W_\infty^{p+1}(V_k \cup V_m)}.$$

That is, if  $u \notin V_h$ , the discrete solution  $u_h$  has a discontinuity proportional to  $h^{p+1}$ , which goes to zero as the space is refined, along the edges of the Voronoi regions. This means that in general the cardinal basis functions also have discontinuities between Voronoi regions. A cardinal function for a one-dimensional problem is shown in Figure 2.

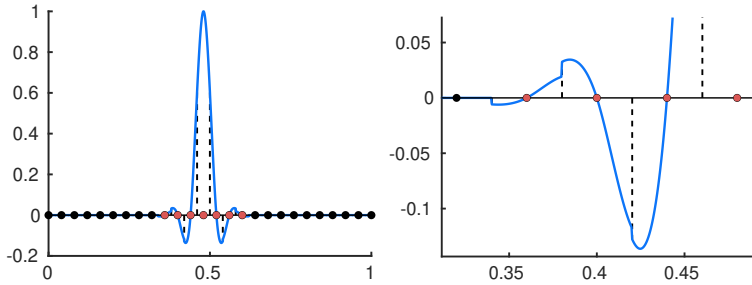


FIG. 2. Left: A cardinal function generated with RBF-FD on a uniform node set in one dimension with stencil size  $n = 7$ . Right: A close up to illustrate the discontinuities at the intersections of the Voronoi regions.

When we use the interpolation error in the global error estimate, we take a norm over the domain. If we let  $\alpha_i = \max_k \alpha_{k,i}$ , we have

$$(4.5) \quad \|\mathcal{L}_i(u_h - u)\|_{\ell_2(\Omega)} \leq \alpha_i h^{p+1-i} |u|_{W_\infty^{p+1}(\Omega)}.$$

For later use, we introduce a piecewise norm over the Voronoi regions  $\|u_h\|_{L_2^*(\Omega)}^2 = \sum_{k=1}^N \|u_h\|_{L_2(V_k \cap \Omega)}^2$ . Note that  $\|\mathcal{L}_i u\|_{L_2^*(\Omega)} = \|\mathcal{L}_i u\|_{L_2(\Omega)}$  for  $u \in W_2^2$ . We have

$$(4.6) \quad \|\mathcal{L}_i(u_h - u)\|_{L_2^*(\Omega)} \leq \alpha_i h^{p+1-i} |u|_{W_\infty^{p+1}(\Omega)}.$$

**4.1. Linear independence of the discrete basis functions.** Since we are solving the least squares problem discretely, we need the cardinal basis functions to be linearly independent not only in the continuous space, but also in the discrete space when they are evaluated at  $y \in Y$ .

**THEOREM 4.1.** *The matrix  $G_E = E_h(Y, X)^T E_h(Y, X)$  is non-singular if the node set  $Y$  is chosen such that in each Voronoi region  $V_i$  of the  $X$  node set, at least one point  $y_j$  is close enough to  $x_i$  for  $\Psi_i(y) > \sum_{j \neq i} |\Psi_j(y)|$  to hold.*

*Proof.* That the matrix  $G_E$  is singular indicates that there exists a non-zero vector  $u_h(X)$  such that  $u_h(X)^T G_E u_h(X) = \|u_h(Y)\|_2^2 = 0$ . That is,  $u_h(y_j) = 0$  for all  $y_j \in Y$ . For any non-zero vector  $u_h(X)$ , there is a maximum value such that  $|u_h(x_i)| \geq |u_h(x_j)|$ . Let  $y_j \in Y$  be an evaluation point located in  $V_i$ , the Voronoi region of  $x_i$ . We first note that  $u_h(y_j) = u_h(x_i) \Psi_i(y_j) + \sum_{m \neq i} u_h(x_m) \Psi_m(y_j)$ . Then we rearrange the terms and take the absolute value:  $|u_h(x_i)| |\Psi_i(y_j)| \leq |u_h(y_j)| + |\sum_{m \neq i} u_h(x_m) \Psi_m(y_j)|$ . Then, for the evaluation point  $y_j$ , we have

$$\begin{aligned} |u_h(y_j)| &\geq |u_h(x_i)| |\Psi_i(y_j)| - \sum_{m \neq i} |u_h(x_m)| |\Psi_m(y_j)| \\ &\geq |u_h(x_i)| (|\Psi_i(y_j)| - \sum_{m \neq i} |\Psi_m(y_j)|). \end{aligned}$$

If  $|\Psi_i(y_j)| > \sum_{m \neq i} |\Psi_m(y_j)|$  then  $|u_h(y_j)| > 0$  and we cannot have singularity. This trivially holds at the data points ( $y_j = x_i$ ), since  $\Psi_j(x_i) = \delta_{ij}$ .  $\square$

In [Figure 3](#), examples of cardinal functions for three different node distributions are shown. We can see that the part of the Voronoi region where the condition of [Theorem 4.1](#) holds is larger for the regular hexagonal node layout, slightly worse for the Halton nodes, and quite small for the random nodes. This means that for irregular nodes, we would need a larger oversampling ratio to guarantee non-singularity. The behavior of the cardinal functions is related to the local interpolation matrices. When the nodes are badly distributed, the local problem is badly conditioned, and the gradients of the local cardinal functions can become large. A pragmatic approach to ensure non-singularity is to select the evaluation points such that the condition is satisfied by construction.

**COROLLARY 4.2.** *If  $X \subset Y$  the matrix  $G_E$  is guaranteed to be non-singular.*

For the theoretical analysis in [section 5](#), we assume that the condition holds for the chosen  $Y$  node set, and for the numerical experiments in [section 6](#), we use the inclusion of  $X$  in  $Y$ . In the latter case, we specifically have

$$(4.7) \quad \|u_h(Y)\|_2 = h_y^{-1} \|u_h(Y)\|_{\ell_2(\Omega)} \geq \|u_h(X)\|_2,$$

which indicates that the smallest singular value of  $E_h$  is bounded from below by 1. In fact, since the identity matrix is a sub-matrix of  $E_h$ , the smallest singular value  $\sigma_{\min}(E_h) = 1$ . We also have  $\|u(Y)\|_2^2 = \|E_h u\|_2^2 = \sum_{i=1}^M (w_i u_i)^2 \leq \max_i \|w_i\|_2^2 \sum_{i=1}^M \|u_i\|_2^2$ , where  $w_i \equiv w_{k(y_i)}^{\mathcal{L}_0}$  and  $u_i \equiv u(X_{k(y_i)})$ . If we use that each

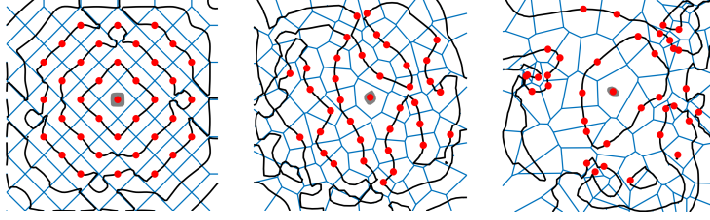


FIG. 3. The unit square is discretized using  $N = 72$  hexagonal node points (left), Halton node points (middle) and random node points (right). In each case, the Voronoi regions and the zero contour lines of the cardinal functions for the central node point are shown. The nodes in the stencil are indicated by a circle and the shaded area is the region where an evaluation point must be placed for non-singularity to be guaranteed. The sizes of the respective regions are approximately 0.017, 0.011, and 0.0078.

function value  $u(x_k)$  appears in  $n$  stencils and each stencil is sampled at most  $cM/N$  times with  $c \approx 1$ , we get  $\|E_h u\|_2^2 \leq \frac{cnM}{N} \max_i \|w_i\|_2^2 \|u\|_2^2$ , and

$$(4.8) \quad \sigma_{\max}(E_h) = \sqrt{cnq} \max_i \|w_{k(y_i)}^{\mathcal{L}_0}\|_2 = \sqrt{cnq} \max_i \left( \sum_{j=1}^N |\Psi_j(y_i)|^2 \right)^{\frac{1}{2}}.$$

**5. Convergence and error estimates for RBF-FD-LS.** In this section, we derive stability, convergence and error estimates for the RBF-FD-LS method. When solving the least squares problem numerically in the form (3.6), we have not experienced practical problems with well-posedness. However, from the theoretical perspective it simplifies the analysis to have the Dirichlet boundary conditions imposed strongly as in (3.17), which means that the error is zero at the node set  $X_{\partial\Omega_0}$ . When performing the analysis, we assume that the weights  $\beta_i = 1$ ,  $i = 0, 1, 2$  in (3.14). Scaling is then discussed separately in subsection 5.5. We first state the global error estimate, and then derive and prove each part of the estimate in the following subsections. The main steps consist of proving coercivity for the continuous bilinear form in a homogeneous space, then relating a piecewise bilinear form to the continuous and showing that it is coercive under a condition on the size of the node distance  $h$ , and finally to show coercivity of the discrete bilinear form under similar conditions on  $h$ .

**5.1. The global error estimate.** To show the global error estimate, we use that  $a_h(u, v)$  is bilinear and symmetric. We also use that

$$(5.1) \quad |a_h(u, v)| \leq \frac{1}{2} a_h(u, u) + \frac{1}{2} a_h(v, v),$$

which holds, since  $|(u, v)| \leq \|u\| \|v\| \leq \frac{1}{2} (\|u\|^2 + \|v\|^2)$  can be applied to each term.

**THEOREM 5.1.** *Consider the least squares problem (3.17) with properties (3.18) and (3.19). If there is an  $h_0$  such that for the trial space error  $e_h = u_h + u_h^0 - I_h(u) \in V_h^0$ , and  $h < h_0$ , it holds that  $a_h(e_h, e_h) \geq \frac{1}{C_h^2} \|e_h\|_{\ell_2}^2$ , then for  $h \leq h_0$ , the error  $e = u_h + u_h^0 - u$  satisfies*

$$(5.2) \quad \|e\|_{\ell_2} \leq C_h \sqrt{2a_h(e_I, e_I)} + \|e_I\|_{\ell_2},$$

where  $e_I = I_h(u) - u$  is the interpolation error.

*Proof.* The error  $e = u_h + u_h^0 - u$  does not lie in the trial space unless  $u$  lies in the trial space. Also,  $u_h + u_h^0$  does not in general interpolate  $u$ . We use the interpolant  $I_h(u) \in V_h$  as an auxiliary function to write  $e = u_h + u_h^0 - u = (u_h + u_h^0 - I_h(u)) + (I_h(u) - u) = e_h + e_I$ . The first term  $e_h$  has nodal values  $e(X)$  and  $e_h \in V_h^0$ , since the Dirichlet condition is imposed strongly. The second term  $e_I$  is the interpolation error, which is not in the trial space. Then

$$(5.3) \quad \|e\|_{\ell_2(\Omega)} = \|e_h + e_I\|_{\ell_2(\Omega)} \leq \|e_h\|_{\ell_2(\Omega)} + \|e_I\|_{\ell_2(\Omega)}.$$

For the error term in the trial space, we start from the assumption that the coercivity property holds, and then use (3.19), (5.1), and (3.18)

$$(5.4) \quad \begin{aligned} \frac{1}{C_h^2} \|e_h\|_{\ell_2}^2 &\leq a_h(e_h, e_h) = a_h(e - e_I, e_h) = a_h(-e_I, e_h) \\ &= a_h(-e_I, e - e_I) = a_h(-e_I, e) + a_h(-e_I, -e_I) \\ &\leq \frac{1}{2} (a_h(e_I, e_I) + a_h(e, e)) + a_h(e_I, e_I) \\ &\leq 2a_h(e_I, e_I), \end{aligned}$$

leading to

$$(5.5) \quad \|e_h\|_{\ell_2} \leq C_h \sqrt{2a_h(e_I, e_I)}.$$

Combining (5.3) and (5.5) provides the final result (5.2).  $\square$

## 5.2. Coercivity of the continuous bilinear form in a homogeneous space.

We introduce a homogeneous auxiliary space  $V^0 = \{u \in V \mid u(y) = 0, y \in \partial\Omega_0\}$  for the continuous least squares problem (2.5). As a step in showing coercivity for the discrete bilinear form, we show coercivity of the continuous bilinear form (2.4) for functions  $u \in V^0 \subset W_2^{p+1}(\Omega)$ .

Given the smoothness assumptions on the domain  $\Omega$  and the function  $u$ , a Poincaré-Friedrich inequality holds with the boundary data given on some part of the boundary [6]. This can be seen if the inequality is shown using integration along paths from points on the Dirichlet boundary to points in the domain.

$$(5.6) \quad \|u\|_{\Omega}^2 \leq C_P^2 (\|u\|_{\partial\Omega_0}^2 + \|\nabla u\|_{\Omega}^2) = C_P^2 \|\nabla u\|_{\Omega}^2.$$

We also need a trace inequality that relates the solution on (any part of) the boundary to the solution in the interior [9]

$$(5.7) \quad \|u\|_{\partial\Omega_i}^2 \leq |\partial\Omega_i|^2 \|u\|_{L^\infty(\partial\Omega_i)}^2 \leq |\partial\Omega_i|^2 C_T^2 (\|u\|_{\Omega}^2 + \|\nabla u\|_{\Omega}^2).$$

Then we have Green's first identity that can be derived from the divergence theorem

$$(5.8) \quad \int_{\Omega} \nabla u \cdot \nabla v = \int_{\partial\Omega} u \frac{\partial v}{\partial n} - \int_{\Omega} u \Delta v$$

leading to

$$(5.9) \quad \begin{aligned} \|\nabla u\|_{\Omega}^2 &\leq \|u\|_{\partial\Omega_0} \|\partial u / \partial n\|_{\partial\Omega_0} + \|u\|_{\partial\Omega_1} \|\partial u / \partial n\|_{\partial\Omega_1} + \|u\|_{\Omega} \|\Delta u\|_{\Omega} \\ &= \|u\|_{\partial\Omega_1} \|\partial u / \partial n\|_{\partial\Omega_1} + \|u\|_{\Omega} \|\Delta u\|_{\Omega}, \end{aligned}$$

where we separated the boundary integral into two parts due to the structure of our specific problem, and used that functions in  $V^0$  vanish on  $\partial\Omega_0$ .

To show coercivity, we start from (5.9), then use the Poincaré inequality (5.6) on the second term, then we use the trace inequality (5.7) on the first term and finally the Poincaré inequality one more time.

$$\begin{aligned}
\|\nabla u\|_\Omega^2 &\leq \|u\|_{\partial\Omega_1} \|\partial u / \partial n\|_{\partial\Omega_1} + \|u\|_\Omega \|\Delta u\|_\Omega \\
&\leq \|u\|_{\partial\Omega_1} \|\partial u / \partial n\|_{\partial\Omega_1} + C_P \|\nabla u\|_\Omega \|\Delta u\|_\Omega \\
&\leq |\partial\Omega_1| C_T (\|u\|_\Omega^2 + \|\nabla u\|_\Omega^2)^{1/2} \|\partial u / \partial n\|_{\partial\Omega_1} + C_P \|\nabla u\|_\Omega \|\Delta u\|_\Omega \\
&\leq |\partial\Omega_1| C_T (C_P^2 \|\nabla u\|_\Omega^2 + \|\nabla u\|_\Omega^2)^{1/2} \|\partial u / \partial n\|_{\partial\Omega_1} + C_P \|\nabla u\|_\Omega \|\Delta u\|_\Omega \\
(5.10) \quad &\leq |\partial\Omega_1| C_T \sqrt{(1 + C_P^2)} \|\nabla u\|_\Omega \|\partial u / \partial n\|_{\partial\Omega_1} + C_P \|\nabla u\|_\Omega \|\Delta u\|_\Omega
\end{aligned}$$

Dividing through by the gradient norm, squaring the result, and using  $(a + b)^2 \leq 2a^2 + 2b^2$  leads to:

$$(5.11) \quad \|\nabla u\|_\Omega^2 \leq 2|\partial\Omega_1|^2 C_T^2 (1 + C_P^2) \|\partial u / \partial n\|_{\partial\Omega_1}^2 + 2C_P^2 \|\Delta u\|_\Omega^2.$$

Let  $C_1^2 = 2|\partial\Omega_1|^2 C_T^2 (1 + C_P^2)$  and  $C_2^2 = 2C_P^2$ . Using (5.6) one more time, we have:

$$(5.12) \quad \|u\|_\Omega^2 \leq C_P^2 \|\nabla u\|_\Omega^2 \leq C_P^2 \max(C_1^2, C_2^2) (\|\partial u / \partial n\|_{\partial\Omega_1}^2 + \|\Delta u\|_\Omega^2).$$

If we finally let  $C^2 = C_P^2 \max(C_1^2, C_2^2)$ , we have the coercivity result

$$(5.13) \quad C^2 a(u, u) \geq \|u\|_\Omega^2, \quad u \in V^0.$$

**5.3. Well-posedness of the discretized PDE problem.** Next, we prove coercivity for functions  $u_h \in V_h^0$  in the piecewise norm defined in section 4. We let

$$(5.14) \quad a^*(u_h, u_h) = \underbrace{\|u_h\|_{L_2^*(\partial\Omega_0)}^2}_{a_0^*(u_h, u_h)} + \underbrace{\|\partial u_h / \partial n\|_{L_2^*(\partial\Omega_1)}^2}_{a_1^*(u_h, u_h)} + \underbrace{\|\Delta u_h\|_{L_2^*(\partial\Omega_0)}^2}_{a_2^*(u_h, u_h)}.$$

The derivation is based on the existence of a function pair  $u_h \in V_h^0$  and  $z \in V_0$ , such that  $u_h = I_h(z)$ , i.e.,  $u_h$  interpolates  $z$ . For a given  $z$ , there is a unique interpolant  $u_h$ , while any  $u_h \in V_h^0$  is the interpolant of a family of functions  $v(u_h) \in V^0$  with the same data at the discrete node set  $X$ . To understand that at least one such function exists, we construct  $v^*(u_h) = \sum_{i=1}^N u_h(x_i) b(\rho_i^{-1} \|x - x_i\|)$ , where  $b(r) \in W_2^{p+1}(\mathbb{R}^2)$  is a bump function with support on the unit disc and with  $b(0) = 1$ . The support radius  $\rho_i = \min(d_X, d_{\partial\Omega})$ , where  $d_X = \min_{j \neq i} \|x_j - x_i\|$  and  $d_{\partial\Omega} = \min_{x \in \partial\Omega} \|x - x_i\|$ . For the proof, we let  $z = \arg \min_{v(u_h)} \|u_h - v\|$ . We start from the continuous bilinear form for  $z$  and then express this as a perturbation of the piecewise bilinear form for  $u_h$ . We bound the perturbations using relation (4.6) for the interpolation error  $u_h - z$ .

$$\begin{aligned}
a(z, z) &= a^*(z, z) = a_1^*(z, z) + a_2^*(z, z) \\
&= \|\partial(z - u_h) / \partial n + \partial u_h / \partial n\|_{L_2^*(\partial\Omega_1)}^2 + \|\Delta(z - u_h) + \Delta u_h\|_{L_2^*(\Omega)}^2 \\
(5.15) \quad &\leq 2a^*(u_h, u_h) - 2\|u_h\|_{L_2^*(\partial\Omega_0)}^2 + 2(\alpha_1 h^p |z|_{W_\infty^{p+1}(\Omega)})^2 + 2(\alpha_2 h^{p-1} |z|_{W_\infty^{p+1}(\Omega)})^2,
\end{aligned}$$

where we used that  $\|a + b\|^2 \leq (\|a\| + \|b\|)^2 \leq 2(\|a\|^2 + \|b\|^2)$ . If we reorganize the terms to look for coercivity of  $a^*(u_h, u_h)$ , and use that  $u_h = u_h - z$  on the Dirichlet boundary, since  $z = 0$  there, we get

$$\begin{aligned}
a^*(u_h, u_h) &\geq \frac{1}{2} a(z, z) + ((\alpha_0 h^{p+1})^2 - (\alpha_1 h^p)^2 - (\alpha_2 h^{p-1})^2) |z|_{W_\infty^{p+1}(\Omega)}^2 \\
(5.16) \quad &\geq \frac{1}{2C^2} \|z\|_\Omega^2 + ((\alpha_0 h^{p+1})^2 - (\alpha_1 h^p)^2 - (\alpha_2 h^{p-1})^2) |z|_{W_\infty^{p+1}(\Omega)}^2.
\end{aligned}$$

Finally, we use  $\|u_h\|_{L_2^*(\Omega)}^2 = \|u_h\|_{L_2(\Omega)}^2 = \|z + u_h - z\|_\Omega^2 \leq 2\|z\|_\Omega^2 + 2\|u_h - z\|_\Omega^2$  to get

$$(5.17) \quad a^*(u_h, u_h) \geq \frac{1}{4C^2} \|u_h\|_\Omega^2 + \left( \left(1 - \frac{1}{2C^2}\right)(\alpha_0 h^{p+1})^2 - (\alpha_1 h^p)^2 - (\alpha_2 h^{p-1})^2 \right) |z|_{W_\infty^{p+1}(\Omega)}^2.$$

If the function  $z$  is well resolved by the step length  $h$ , then the error terms are small compared with the norms of  $z$  and  $u_h$ , and we can bound the bilinear form.

**THEOREM 5.2.** *For a given function  $z \in V^0$ , interpolated by  $u_h \in V_h^0$  on a node set with a fill distance  $h$  and a separation distance  $s \geq c_s h$  there is an  $h_0$  such that*

$$(5.18) \quad a^*(u_h, u_h) \geq \frac{1}{8C^2} \|u_h\|_\Omega^2, \quad \forall h \leq h_0, \quad u_h = I_h(z) \in V_h^0, \quad z \in V^0.$$

*Proof.* Since the function  $z$  is fixed,  $|z|_{W_\infty^{p+1}(\Omega)}$  in (5.16) is also fixed. The constants  $\alpha_i$  depend on the quality of the node distribution, which is why the condition on the relation between fill distance and separation distance is needed. Then we can bound the errors for the sequence of node distributions with the worst case  $\alpha_i$ . As  $h \rightarrow 0$ , the magnitude of the two (or three if  $C^2 < 0.5$ ) negative terms  $(\alpha_1 h^p)^2 + (\alpha_2 h^{p-1})^2 \rightarrow 0$ . There is an  $h_0$  where the absolute value of the sum of the negative correction terms is smaller than  $\frac{1}{8C^2} \|u_h\|^2$ . Then  $\|u_h\|_{L_2^*(\Omega)} \approx \|z\|_\Omega$ , and if we assume that the third correction term is the largest,

$$(5.19) \quad h_0 \approx \left( \frac{\|z\|_\Omega}{\sqrt{8C}\alpha_2 |z|_{W_\infty^{p+1}(\Omega)}} \right)^{\frac{1}{p-1}}. \quad \square$$

**5.4. Well-posedness in the discrete norm.** The discrete  $\ell_2$ -norm on the set of nodes  $Y = \{y_i\}_{i=1}^M$  is an approximation of the piecewise  $L_2^*$ -norm. The last step in the coercivity proof consists of quantifying the difference. We can generally write

$$(5.20) \quad \mathcal{I} = \int_\Omega f(y) dy = \frac{|\Omega|}{M} \sum_{i=1}^M f(y_i) + \gamma_I(f) = \mathcal{I}_h + \gamma_I(f).$$

We want to use this relation for non-trivial domains, which means that we need to consider scattered nodes. Even if the nodes are regular in parts of the domain, they need to be somewhat irregular near the boundary. A very general error estimate for scattered node quadrature is given by

$$(5.21) \quad |\gamma_I(f)| \leq D_M(Y) V(f),$$

where  $D_M(Y)$  is the star discrepancy of the node set and  $V(f)$  is the Hardy-Krause variation of  $f$  [1]. This has been shown for general domains and piecewise smooth functions in [7, 8]. Both of the factors in (5.21) are hard to quantify in general. However, the standard deviation of the error for an arbitrary node layout (Monte Carlo integration) in practical cases decreases as  $\mathcal{O}(1/\sqrt{M})$  and for a low discrepancy (quasi random) node layout, it decreases as  $\mathcal{O}((\log M)^d/M)$ . The standard deviation can be interpreted as a relative error. That is, we can write

$$(5.22) \quad (1 - c\tilde{\gamma}_I(f))\mathcal{I} \leq \mathcal{I}_h \leq (1 + c\tilde{\gamma}_I(f))\mathcal{I},$$

where  $\tilde{\gamma}_I$  is the standard deviation and  $c > 0$  is a constant.

In our model problem, we have one-dimensional and two-dimensional integrals. If the layout of the evaluation node points is quasi uniform on the boundary, then the error in these integrals is  $\mathcal{O}(h_y)$ , since in this case, they represent the usual Riemann sum. In the interior, without specific assumptions on the nodes, the error is also at most  $\mathcal{O}(h_y)$ , since  $h_y \propto M^{-1/2}$ .

If  $c_a(u)h_y$  is the largest integration error in the three piecewise integrals that  $a_h(u_h, u_h)$  consist of, then:

$$(5.23) \quad a_h(u_h, u_h) \geq (1 - c_a(u)h_y)a^*(u_h, u_h).$$

If we in the same way denote the error in the squared norm over the domain by  $c_n h_y$ , we have

$$(5.24) \quad \|u_h\|_{\ell_2(\Omega)}^2 \leq (1 + c_n h_y) \|u_h\|_{L_2(\Omega)}^2.$$

Combining (5.18), (5.23), and (5.24), leads to

$$(5.25) \quad \begin{aligned} \|u_h\|_{\ell_2(\Omega)}^2 &\leq (1 + c_n h_y) \|u_h\|_{L_2(\Omega)}^2 \\ &\leq (1 + c_n h_y) 8C^2 a^*(u_h, u_h) \leq \frac{(1 + c_n(u)h_y)}{(1 - c_a(u)h_y)} 8C^2 a_h(u_h, u_h). \end{aligned}$$

This shows that as long as the relative integration error in the bilinear form is less than unity, the coercivity of the discrete bilinear form follows from that of the piecewise continuous bilinear form for functions in the trial space. We also note that the left hand side is positive as long as  $u_h$  is non-zero as shown in [Theorem 4.1](#). The coercivity constant  $C_h$  needed in [Theorem 5.1](#), extracted from (5.25) is

$$(5.26) \quad C_h \equiv \sqrt{8}CC_I = \sqrt{8}C \left( \frac{(1 + c_n(u)h_y)}{(1 - c_a(u)h_y)} \right)^{\frac{1}{2}}.$$

**COROLLARY 5.3.** *Given estimate (5.25), we have the relation*

$$(5.27) \quad \sigma_{\min}(\bar{D}_h(Y, \tilde{X})) \geq \sigma_{\min}(\bar{E}_h(Y, \tilde{X}))/C_h.$$

*Proof.* Let  $u = u_h(\tilde{X})$  be any vector for which it holds that  $\|u\|_2 = 1$ . Then  $(\sigma_{\min}(\bar{E}_h))^2 \leq u^T \bar{E}_h^T \bar{E}_h u = \|u_h\|_{\ell_2}^2 \leq C_h^2 a_h(u_h, u_h) = C_h^2 u^T \bar{D}_h^T \bar{D}_h u$ .  $\square$

**5.5. Discussion of the global error estimate including scaling.** All the components of the global error estimate are now in place, and we can discuss their properties as well as the question about scaling of the different terms in the bilinear form. Equation (4.5) for the interpolation error  $e_I = I_h(u) - u$  yields

$$(5.28) \quad \|e_I\|_{\ell_2} \leq \alpha_0 h^{p+1} |u|_{W_{\infty}^{p+1}(\Omega)},$$

and for the bilinear form applied to the interpolation error we have

$$(5.29) \quad a_h(e_I, e_I) \leq ((\alpha_0 h^{p+1})^2 + (\alpha_1 h^p)^2 + (\alpha_2 h^{p-1})^2) |u|_{W_{\infty}^{p+1}(\Omega)}^2.$$

Noting that  $a^2 + b^2 + c^2 \leq (a + b + c)^2$  for positive numbers, we insert all terms in the global error estimate (5.2), to get

$$(5.30) \quad \|e\|_{\ell_2} \leq 4C \left( \frac{(1 + c_n(u)h_y)}{(1 - c_a(u)h_y)} \right)^{\frac{1}{2}} (\tilde{\alpha}_0 h^{p+1} + \alpha_1 h^p + \alpha_2 h^{p-1}) |u|_{W_{\infty}^{p+1}(\Omega)},$$

where  $\tilde{\alpha}_0 = \alpha_0(1 + \frac{1}{4C})$  incorporates the last interpolation error term. The most important aspect to discuss is the notion of  $h$  being small enough. We know that the coercivity property of the discretized problem (5.18) holds for  $h < h_0$ , which indicates that the function it is being applied to is well resolved. In Theorem 5.1 we use the coercivity property for  $e_h = u_h - I_h(u)$ . Generally, we can say that the trial space error and its components are well resolved if  $u$  is well resolved, since  $u_h$ , to some extent, and  $I_h(u)$  derive their properties from  $u$ . That is, we can apply condition (5.19) to  $u$  to understand what is an appropriate size of the node distance  $h$ .

We also need  $h_y$  to be small enough that the discrete norm is close enough to the continuous norm. We need  $c_a h_y < 1$  for the estimate to be valid. If  $c_a h_y$  is close to unity, the factor that depends on  $h_y$  decreases rapidly when the oversampling is increased, while asymptotically, the factor reduces linearly with  $h_y$ . Integration has a smoothing effect, and our experience from the experiments is that  $h_y < h$  is sufficient for the estimate to hold if  $h$  resolves  $u$ , while the accuracy benefits from more oversampling.

The error expression (5.30) indicates that depending on the balance of the three error terms and the range of  $h$ , the final convergence rate is between  $p - 1$  and  $p + 1$ . The balance can be changed through the scale factors  $\beta_i$  in (3.14). The scale factors in turn affect the stability constant. The scaled error estimate takes the form:

$$(5.31) \quad \|e\|_{\ell_2} \leq 4C_\beta C_{\mathcal{I}} \left( \left( \beta_0 + \frac{1}{4C_\beta} \right) \alpha_0 h^{p+1} + \beta_1 \alpha_1 h^p + \beta_2 \alpha_2 h^{p-1} \right) |u|_{W_\infty^{p+1}(\Omega)},$$

where the scaled stability constant is given by

$$(5.32) \quad C_\beta = \sqrt{2}C_P \max \left( \frac{|\partial\Omega_1|C_T\sqrt{1+C_P^2}}{\beta_1}, \frac{C_P}{\beta_2} \right) = \sqrt{2}C_P \max \left( \frac{C_1}{\beta_1}, \frac{C_2}{\beta_2} \right).$$

At least in the theoretical estimate, the stability is determined by the constant associated with the Neumann term in the unscaled bilinear form. This indicates that it can be beneficial to choose  $\beta_1 = 1$  and  $\beta_2 = C_2/C_1$  to reduce the residual contribution from the Laplacian part when this is the largest.

The scaling  $\beta_0$  of the Dirichlet condition does not affect  $C_\beta$  directly, but we can see from (5.16) that the stability (in terms of the constant in front of  $C_\beta$ ) is improved if the term corresponding to the Dirichlet condition is larger in relation to the terms corresponding to the Neumann and Laplace equations. The largest scaling such that the order of the Dirichlet term does not dominate the order of the Neumann term is  $\beta_0 = \mathcal{O}(h^{-1})$ . This scaling strategy is evaluated numerically in section 6 and is shown to perform well.

**6. Numerical study.** In this section, we investigate the convergence, stability, and efficiency of RBF-FD-LS compared with collocation-based RBF-FD (RBF-FD-C). We solve the PDE problem (2.1) using the scaling (3.14) with  $\beta_0 = h^{-1}/\sqrt{|\partial\Omega_0|}$ ,  $\beta_1 = 1/\sqrt{|\partial\Omega_1|}$ , and  $\beta_2 = 1/\sqrt{|\Omega|}$  on a domain with an outer boundary defined in polar coordinates as

$$(6.1) \quad r(\theta) = 1 + \frac{1}{10} \left( \sin(7\theta) + \sin(\theta) \right), \quad \theta \in [-\pi, \pi),$$

and with the Dirichlet boundary  $\partial\Omega_0$  defined by  $r(\theta)$ ,  $\theta \in [-\pi, 0)$  and the Neumann boundary  $\partial\Omega_1$  defined by  $r(\theta)$ ,  $\theta \in [0, \pi)$ . The node sets  $X$  and  $Y$  are generated using *DistMesh* [19]. However, in order to enforce  $X \subset Y$  (see subsection 4.1), we

modify the  $Y$  node set such that for each  $x_k \in X$  we find the closest point  $\tilde{y}_j$  in the initial node set  $\tilde{Y}$ , and then let  $y_j = x_k$  in the final node set  $Y$ . The Dirichlet boundary conditions are enforced exactly at  $X_{\partial\Omega_0}$  according to (3.17). The domain  $\Omega$ , an example of the spatial error distribution, the node sets  $X$  and  $Y$ , and the Voronoi diagram corresponding to the node set  $X$  are shown in Figure 4. All experiments were run in MATLAB on a laptop with an Intel i7-7500U processor and 16 GB of RAM.

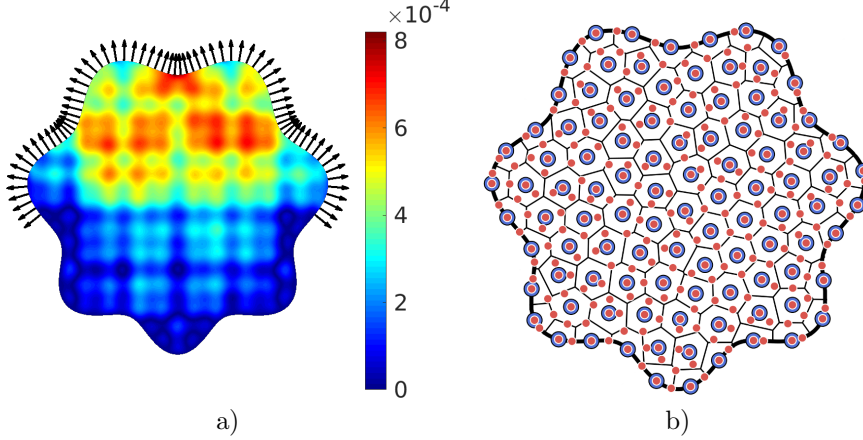


FIG. 4. a) A contour plot of the absolute error distribution over the domain  $\Omega$  for the truncated Non-analytic solution function (6.6) when  $h = 0.02$ ,  $p = 3$ ,  $q = 3$ . The outward normals indicate the locations where the Neumann condition is enforced. b) The  $X$  node set (large blue markers) and the  $Y$  node set (small red markers) are shown together with the Voronoi diagram for the  $X$  node set. Each Voronoi cell contains on average three  $Y$  node points.

In the numerical study we focus on the three main method parameters: The node distance  $h$ , the oversampling parameter  $q = \frac{M}{N} = (h/h_y)^2$ , which determines  $h_y$ , and the polynomial degree  $p$ . When nothing else is stated, we use the default value  $q = 3$  for the oversampling. The stencil size in all experiments is  $n = 2m$ , where  $m$  is the dimension of the polynomial space. In the convergence experiments, we measure the relative  $\ell_2$ -error

$$(6.2) \quad \|e\| = \frac{\|u_h(Y) - u(Y)\|_{\ell_2}}{\|u(Y)\|_{\ell_2}}.$$

We also investigate the stability norm, which we define as the ratio of the largest singular value of  $\bar{E}_h(Y, \tilde{X})$  and the smallest singular value of  $\bar{D}_h(Y, \tilde{X})$ . The stability norm provides a numerical value for the coercivity constant  $C_h$  in the global error estimate (5.2). Using (3.17) for the interior solution, we have

$$(6.3) \quad \begin{aligned} \|u_h(Y)\|_{\ell_2} &= \|\bar{E}_h(Y, \tilde{X}) u(\tilde{X})\|_2 = \|\bar{E}_h \bar{D}_h^+ \tilde{F}(Y)\|_2 \\ &\leq \|\bar{E}_h\|_2 \|\bar{D}_h^+\|_2 \|\tilde{F}(Y)\|_2 = \frac{\sigma_{\max}(\bar{E}_h)}{\sigma_{\min}(\bar{D}_h)} \|\tilde{F}(Y)\|_2. \end{aligned}$$

Combining the estimates (4.8) and (5.27) with  $\sigma_{\min}(E_h) = 1$  yields

$$(6.4) \quad \frac{\sigma_{\max}(\bar{E}_h)}{\sigma_{\min}(\bar{D}_h)} \leq \tilde{c} \sqrt{q} C_h \sqrt{n} \max_i \left( \sum_{j=1}^N |\Psi_j(y_i)|^2 \right)^{\frac{1}{2}}.$$

**6.1. Errors and convergence tests for different functions.** Three solution functions which are different in nature are used to compute the right-hand-side data of (2.1). The purpose of this test is to show the differences in the error behavior and to pick one solution function for which the method is later on tested more extensively. Additionally, we solve the PDE problem with only Dirichlet boundary data. The following functions are considered:

$$(6.5) \quad u_1(x, y) = \sqrt{x^2 + y^2},$$

$$(6.6) \quad u_2(x, y) = \sum_{k=0}^5 e^{-\sqrt{2}^k} (\cos(2^k x) + \cos(2^k y)),$$

$$(6.7) \quad u_3(x, y) = \sin(2(x - 0.1)^2) \cos((x - 0.3)^2) + \frac{\sin(2(y - 0.5)^2)^2}{1 + 2x^2 + y^2},$$

which are referred to by the following names: Distance, truncated Non-analytic and Rational sine, respectively. The polynomial degree  $p = 5$  is used for computing the local interpolation matrices. The error under refinement of  $h$  is displayed in Figure 5.

The accuracy of RBF-FD-LS is better than that of RBF-FD-C for all solution functions when both the Neumann and Dirichlet conditions are present. The convergence rates for the truncated Non-analytic and Rational sine functions are  $k = 4.4$  and  $k = 4.8$  respectively, which agrees with the error estimate (5.30) since  $k \geq p - 1 = 4$ . The convergence rate for the Distance function is  $k = 1.4 < 4$ , but that is expected since it is a  $C^0$  function.

When only the Dirichlet condition is imposed, the accuracy of RBF-FD-LS is better for the Distance and Rational sine functions. This is also the case for the truncated Non-analytic function, when  $h$  is small enough. The difference in error between RBF-FD-LS and RBF-FD-C is not as large as when both the Neumann and Dirichlet conditions are imposed. Also in this case the convergence rates for the truncated Non-analytic function and Rational sine function are  $k \geq p - 1 = 4$ .

In the following subsections further experiments are made with the truncated Non-analytic solution function, which due to its fine scale variation is challenging to approximate.

**6.2. Approximation properties under node refinement.** We refine  $h$  (this increases the number of nodes  $N$ ), and measure the approximation properties for different polynomial degrees in the local interpolation matrices (1.5). We denote this by  $h$ -refinement. The convergence as a function of the node distance is shown in Figure 6. We observe that the accuracy of RBF-FD-LS is better for each tested  $p$  compared with RBF-FD-C. The overall difference in the errors is larger for  $p = 5$  compared with when  $p = 3$  and 4. The convergence trend  $k$  of RBF-FD-LS is  $k \geq p - 1$  for every  $p$ . It is hard to evaluate the convergence trend of RBF-FD-C since the error behavior is unpredictable.

Next, the relation between the error and the computational time (runtime) is investigated. It is important to note that a method with a smaller error/runtime ratio is more efficient. The runtime is taken to be a sum of the following steps in the execution:

- Generation of the local matrices: the closest neighbor search, forming and inverting the local interpolation matrices (1.5), forming the evaluation and differentiation weights (3.3).
- Assembly of the PDE operator (3.4).

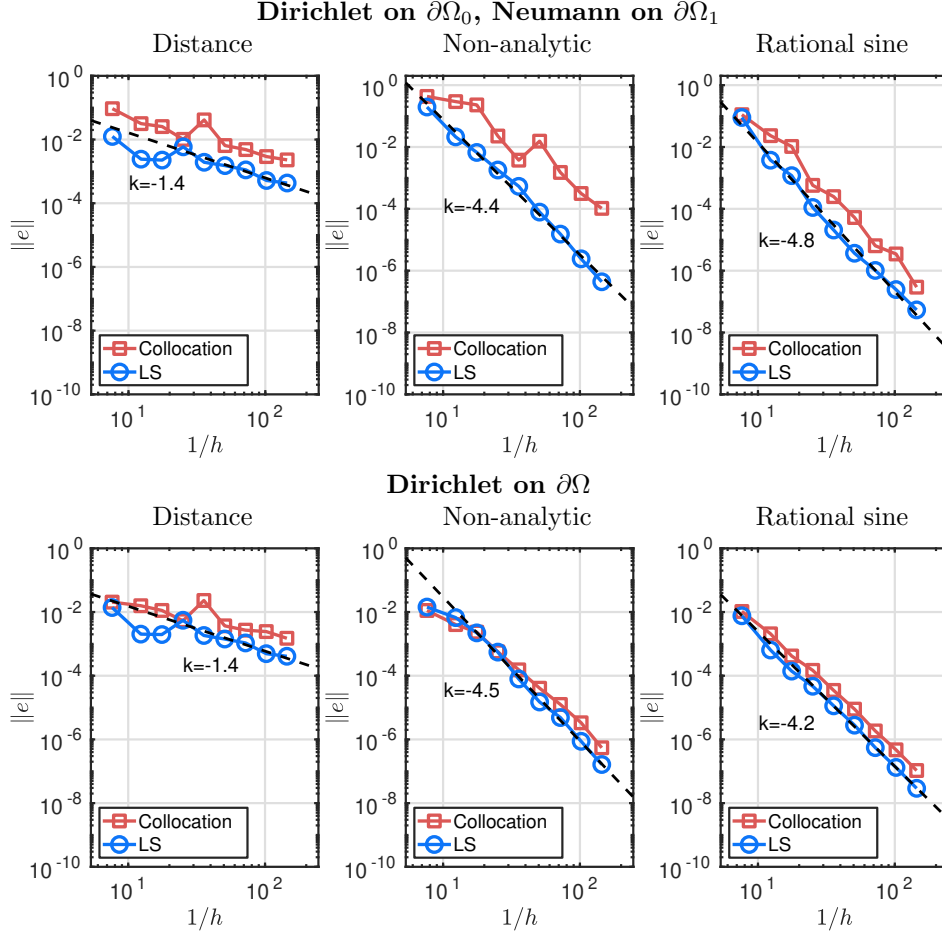


FIG. 5. The errors of RBF-FD-LS and RBF-FD-C as a function of the inverse node distance for the three different solution functions defined in subsection 6.1. The first row of plots corresponds to solving (2.1) and the second row corresponds to solving the same problem with the Dirichlet condition on the whole boundary. The polynomial degree used to construct the interpolation matrices is  $p = 5$  and the oversampling parameter  $q = 3$ . The number of node points in  $X$  ranges from  $N = 500$  to  $N = 64000$ .

- Solution to the system of equations using `mldivide()` in MATLAB.

The node generation is considered as a preprocessing step and is therefore not included in the measurement. The error as a function of runtime is given in Figure 7. We observe that the efficiency of RBF-FD-LS is better than that of RBF-FD-C for all considered  $p$ . When  $p = 5$ , the difference in the efficiency is larger. The oversampling parameter  $q$  does not have a decisive role when it comes to the efficiency. We expect the run-time to be dominated by the solution of the overdetermined linear system. For a dense matrix, the cost grows linearly with  $M = qN$  for a fixed  $N$ . We expect a similar behavior for our sparse system. The added cost is compensated for by the improved accuracy. Figure 10 shows the error improvement with  $q$ .

The stability norm (6.4) as a function of  $1/h$  is studied in Figure 8. Here we can observe that the stability norm of RBF-FD-LS is almost constant for all polynomial degrees  $p$  which we considered. This corresponds with the error estimate (5.30) since

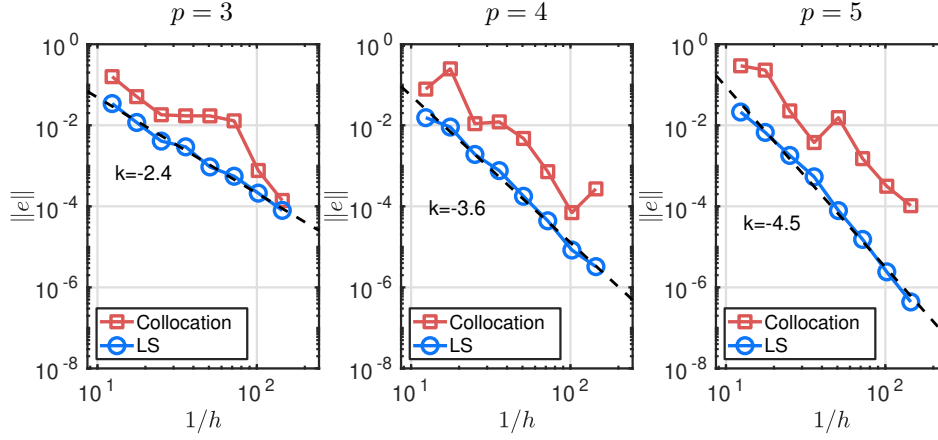


FIG. 6. The RBF-FD-LS and RBF-FD-C methods are compared. The relative error as a function of the inverse node distance  $1/h$  for a fixed oversampling parameter  $q = 3$  and different polynomial degrees  $p$  used to form the local interpolation matrices.

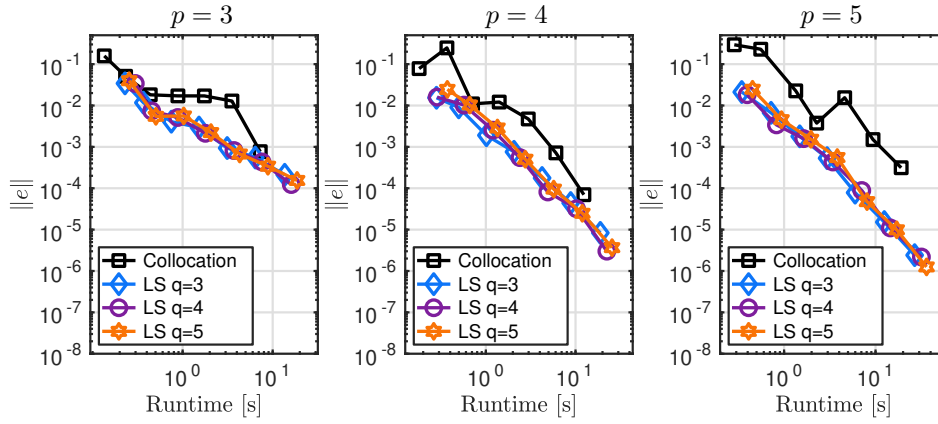


FIG. 7. The RBF-FD-LS and RBF-FD-C methods are compared. The relative error as a function of the runtime measured in seconds for a fixed oversampling parameter  $q = 3$  and different polynomial degrees  $p$  used to form the local interpolation matrices.

the stability constant  $C_h$  from (5.26) takes the form  $C_h = \sqrt{8}C \left( \frac{(1+c_n(u)h_y)}{(1-c_a(u)h_y)} \right)^{\frac{1}{2}}$  and under  $h$ -refinement we have that  $h_y = \frac{1}{\sqrt{q}} h$ . It follows that when  $q$  is fixed and  $h$  is small enough  $C_h \approx \sqrt{8}C$  does not change with  $h$  anymore, thus the stability norm (6.4) is constant. The stability norm of the RBF-FD collocation method does not follow a pattern for the given PDE, parameters and node sets. Here we emphasize that this behavior is not caused by the RBF-FD trial space, but rather by the collocation formulation in which the PDE is solved.

The condition number of a rectangular or square matrix  $A$  is defined by  $\kappa(A) = \|A\|_2 \|A^+\|_2 = \sigma_{\max}(A)/\sigma_{\min}(A)$ . In Figure 9 we show the condition numbers for the two matrices involved in RBF-FD-LS:  $\bar{D}_h$  and  $E_h$ . We observe that  $\kappa(\bar{D}_h)$  grows with  $\frac{1}{h^2}$  for  $p = 3$ . The results are almost identical for  $p = 4$  and  $5$ . This is an expected (optimal) growth, since  $\bar{D}_h$  is a numerical second-order differentiation operator, which

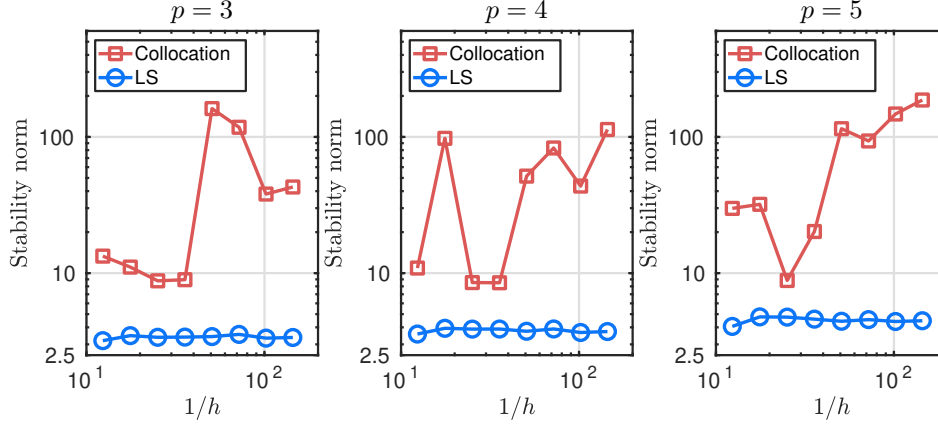


FIG. 8. The stability norm (6.4) as a function of  $1/h$  when the oversampling parameter is  $q = 3$  for different polynomial degrees  $p$ .

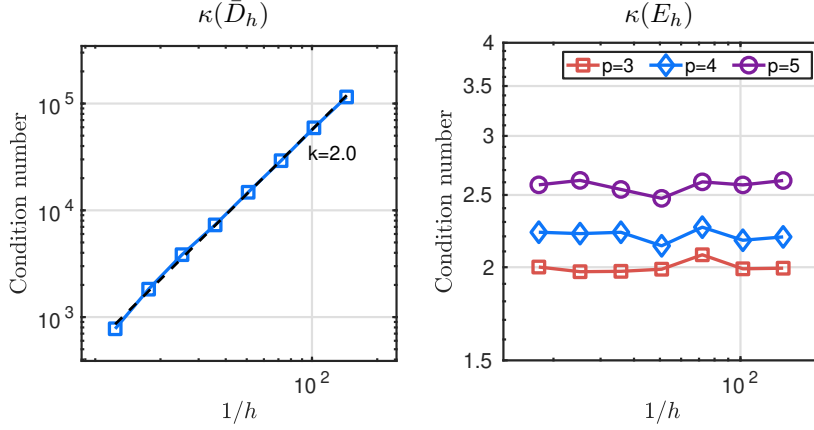


FIG. 9. Left: the condition number of the PDE matrix  $\bar{D}_h$  as a function of the inverse node distance when the polynomial degree used for representing the trial space is  $p = 3$ . Right: the condition number of the evaluation matrix  $E_h$  when the polynomial degrees used for representing the trial space are  $p = 3, 4$  and  $5$ .

has an inverse quadratic dependence on  $h$  when the stencil size is kept constant. On the other hand  $\kappa(E_h)$  is constant with respect to  $h$  for all  $p$ , which is an expected result, since  $E_h$  is a numerical interpolation operator, which does not by itself yield a dependence on  $h$  when the stencil size is kept constant.

**6.3. Approximation properties as the oversampling is increased.** In this section we build understanding of the error and stability behavior for different choices of  $h_y = h/\sqrt{q}$ , when  $h$  is fixed at  $h = 0.08$  (under-resolved case) and at  $h = 0.02$  (well-resolved case). Three polynomial degrees  $p = 3, 4$  and  $5$  are used for the local interpolation matrices (1.5). The exact solution is chosen to be the truncated Non-analytic function (6.6). The convergence study is displayed in Figure 10. For both, the under-resolved and well-resolved cases, the error decays rapidly and then levels out as  $h_y$  becomes small enough. This behavior matches the error estimate (5.30) for

the case when  $h$  is fixed. As  $h_y \rightarrow 0$  the term  $\left(\frac{1+c_n h_y}{1-c_a h_y}\right)^{\frac{1}{2}} \rightarrow 1$  from a larger value, and therefore  $\|e\|_{\ell_2}$  levels out. The stability norm behavior is shown in Figure 11, from

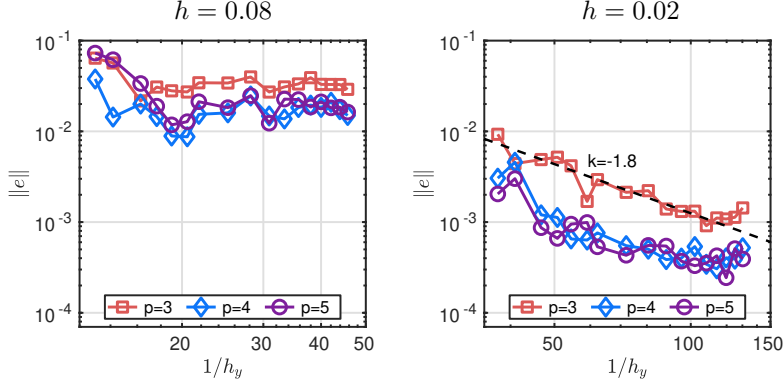


FIG. 10. The error against  $1/h_y$  which is the average distance in the  $Y$  node set for different choices of the polynomial degree  $p$  used to form the trial space. The average internodal distance in the node set  $X$ , was for the left plot fixed at  $h = 0.08$  and for the right plot fixed and  $h = 0.02$ . The values of  $h_y$  were computed from  $q = (1.1, 1.3, 1.7, 2, 2.3, 2.7, 3, 3.3, 3.7, 4, 5, 6, 7, 8, 9, 10, 11)$ .

which we observe that in both the well-resolved and under-resolved cases, the norm first rapidly decays and then flattens out when  $h_y$  is small enough. The approximate point when the stability norm starts to flatten out is at  $1/h_y \approx 28$  (corresponding to  $q = 3.7$ ) for the under-resolved case and at  $1/h_y \approx 70$  ( $q = 3.3$ ) for the well-resolved case.

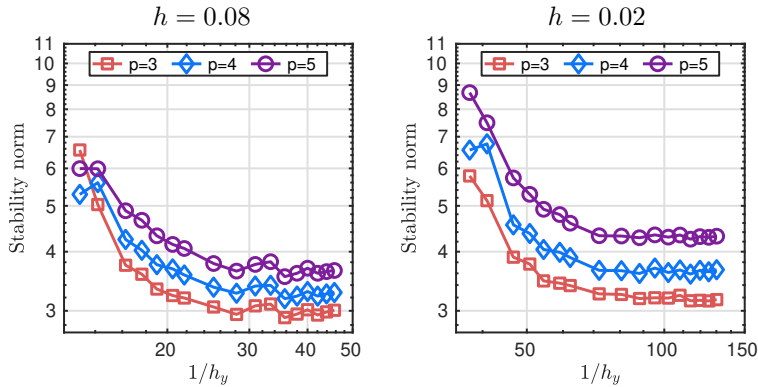


FIG. 11. Both plots show the stability norm (6.4) as a function of  $1/h_y$ , the average inverse node distance in the point set  $Y$ . Different choices of the polynomial degree  $p$  were used to form the trial space. The average internodal distance  $h$  in the node set  $X$ , was for the left plot fixed at  $h = 0.08$  and for the right plot fixed and  $h = 0.02$ , illustrating the under-resolved and the well-resolved case. The values of  $h_y$  were computed from  $q = (1.1, 1.3, 1.7, 2, 2.3, 2.7, 3, 3.3, 3.7, 4, 5, 6, 7, 8, 9, 10, 11)$ .

#### 6.4. Approximation properties as the polynomial degree is increased.

Here we increase the number of points per stencil, together with increasing the polynomial degree  $p$  used to form the stencil-based interpolant (1.5), while the distance  $h$  between the stencil points is kept the same. This is denoted by  $p$ -refinement. We con-

sider polynomial degrees up to  $p = 12$  in order to test the limits of the method. Two different solution functions are considered, the truncated Non-analytic function (6.6) and the Rational sine function (6.7). The least-squares and collocation approaches are compared when  $h$  is fixed at  $h = 0.08$  (under-resolved case) and at  $h = 0.02$  (well-resolved case). A key observation from the results in Figure 12 is that the error for

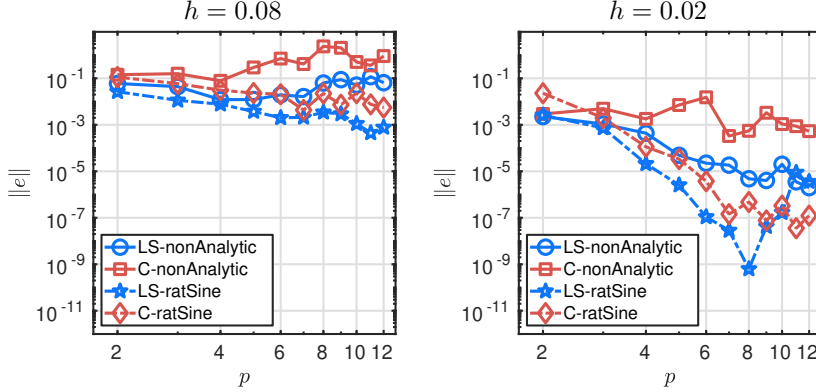


FIG. 12. The relative error in the  $p$ -refinement mode: the polynomial degree used to form the stencil-based interpolation matrix (1.5) is increased, while the internodal distance between the stencil points is fixed at  $h = 0.08$  and  $h = 0.02$ .

both resolutions and both manufactured solutions is smaller for RBF-FD-LS than for RBF-FD-C. For the under-resolved case ( $h = 0.08$ ), there is some improvement of the error when increasing  $p$  for the Rational sine function. The results are worse for the truncated Non-analytic function that has large derivatives and requires higher resolution. In this case, the error increases for  $p > 4$ . In the well-resolved case ( $h = 0.02$ ), we observe convergence with  $p$  in all cases except RBF-FD-C for the Non-analytic function. For  $p \geq 8$ , round-off errors prevent further convergence for RBF-FD-LS. The convergence trend for RBF-FD-C levels out earlier than for RBF-FD-LS.

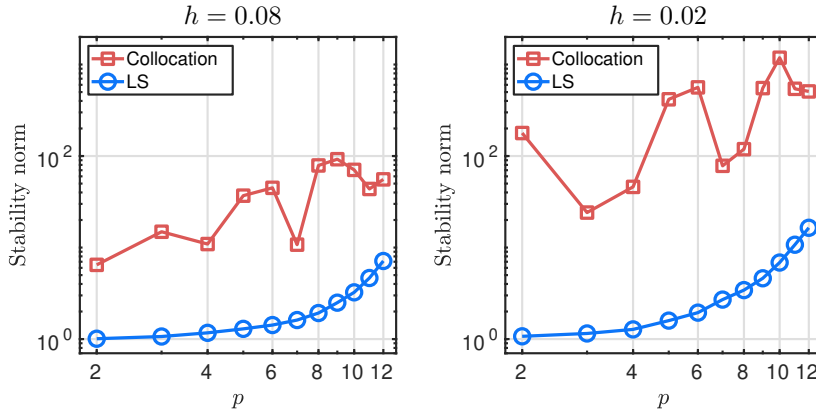


FIG. 13. The stability norm in the  $p$ -refinement mode: the polynomial degree used to form the stencil-based interpolation matrix (1.5) is increased, while the internodal distance between the stencil points  $h$  is fixed at  $h = 0.08$  and  $h = 0.02$ .

The stability norm as a function of  $p$  is shown in Figure 13. It has an increasing

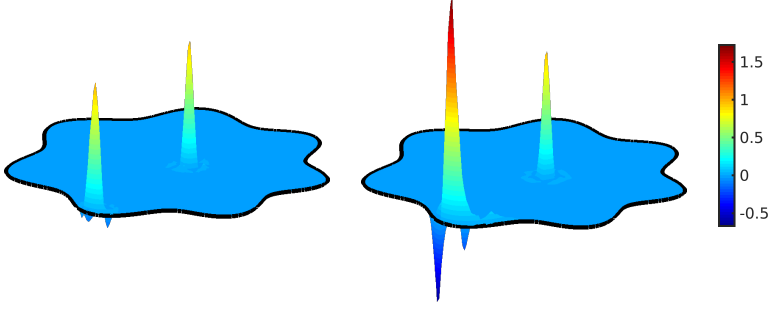


FIG. 14. Example of two cardinal functions placed on the boundary of  $\Omega$  and in the interior of  $\Omega$  for  $p = 3$  (left) and  $p = 12$  (right). For both cases the internodal distance is  $h = 0.06$ .

trend for both methods. Based on the estimate (6.4), we expect the numerator to grow with  $\sqrt{n} \approx p$  and with the norm of the weights. In the ideal case, the maximum value for any cardinal function is one, but here, there is an exponential growth of these functions with  $p$ , especially for cardinal functions close to the boundary. The largest weight for  $p = 12$  has  $|w| \approx 3.2$ . Cardinal functions for different values of  $p$  are illustrated in Figure 14. The condition numbers of the local interpolation matrices  $\tilde{A}_k$  also grow exponentially with  $p$ , and for  $p \gtrsim 12$  prevent accurate numerical evaluation of the weights.

**7. Final remarks.** In this paper we introduced an enhancement of the collocation based RBF-FD method where we instead use a least-squares approach. The main method parameters are the node distance  $h$ , the evaluation node distance  $h_y$ , and the polynomial degree  $p$  used to form the stencil approximations. The least squares formulation led us to characterize the RBF-FD trial space as a piecewise continuous space with jumps that vanish together with the local approximation error, and to understand that  $\tilde{D}_h^T \tilde{D}_h u = \tilde{D}_h^T f$  reproduces the  $L_2$  inner-products of the continuous least-squares problem up to an error of size  $O(h_y)$ . This allowed us to prove well-posedness (stability) of RBF-FD-LS for an elliptic problem as  $h_y \rightarrow 0$  when  $h$  is small enough. We also derived an error estimate in terms of the node distance, where the error decays with no less than order  $p - 1$  for the Poisson problem with Dirichlet and Neumann boundary conditions. The estimate showed that taking  $h_y = h_y(h)$ , such that  $h_y < h$ , enables convergence  $u_h \rightarrow u$  as  $h \rightarrow 0$ .

The experiments confirmed the theoretical observations in terms of the convergence trend as  $h \rightarrow 0$ . We also confirmed that as  $h$  is fixed at a small value, the stability norm and the error are improved as  $h_y \rightarrow 0$ , until both level out. This happens when the effect of the numerical integration becomes negligible.

Furthermore, the numerical experiments indicated that RBF-FD-LS for our model problem performs better than RBF-FD-C in terms of:

- the error against the exact solution for  $p$ -refinement and  $h$ -refinement,
- the stability properties,
- the efficiency.

The most important strength of the least-squares formulation is the robustness of the numerical solution as  $h \rightarrow 0$ , which, according to our experience, is often lacking in the collocation formulation, especially in the presence of Neumann boundary conditions.

**Acknowledgments.** For valuable discussions we thank Murtazo Nazarov, Gunnilla Kreiss and Eva Breznik from Uppsala University.

## REFERENCES

- [1] C. AISTLEITNER, F. PAUSINGER, A. M. SVANE, AND R. F. TICHY, *On functions of bounded variation*, Math. Proc. Cambridge Philos. Soc., 162 (2017), pp. 405–418, <https://doi.org/10.1017/S0305004116000633>.
- [2] G. A. BARNETT, *A Robust RBF-FD Formulation based on Polyharmonic Splines and Polynomials*, Ph.D. thesis, University of Colorado at Boulder, Dept. of Applied Mathematics, Boulder, CO, USA, 2015.
- [3] V. BAYONA, *An insight into RBF-FD approximations augmented with polynomials*, Comput. Math. Appl., 77 (2019), pp. 2337–2353, <https://doi.org/10.1016/j.camwa.2018.12.029>.
- [4] V. BAYONA, N. FLYER, AND B. FORNBERG, *On the role of polynomials in RBF-FD approximations: III. Behavior near domain boundaries*, J. Comput. Phys., 380 (2019), pp. 378–399, <https://doi.org/10.1016/j.jcp.2018.12.013>.
- [5] V. BAYONA, N. FLYER, B. FORNBERG, AND G. A. BARNETT, *On the role of polynomials in RBF-FD approximations: II. Numerical solution of elliptic PDEs*, J. Comput. Phys., 332 (2017), pp. 257–273, <https://doi.org/10.1016/j.jcp.2016.12.008>.
- [6] A. BOULKHEMAIR AND A. CHAKIB, *On the uniform Poincaré inequality*, Comm. Partial Differential Equations, 32 (2007), pp. 1439–1447, <https://doi.org/10.1080/03605300600910241>.
- [7] L. BRANDOLINI, L. COLZANI, G. GIGANTE, AND G. TRAVAGLINI, *A Koksma-Hlawka inequality for simplices*, in Trends in harmonic analysis, vol. 3 of Springer INdAM Ser., Springer, Milan, 2013, pp. 33–46, [https://doi.org/10.1007/978-88-470-2853-1\\_3](https://doi.org/10.1007/978-88-470-2853-1_3).
- [8] L. BRANDOLINI, L. COLZANI, G. GIGANTE, AND G. TRAVAGLINI, *On the Koksma-Hlawka inequality*, J. Complexity, 29 (2013), pp. 158–172, <https://doi.org/10.1016/j.jco.2012.10.003>.
- [9] A. CIANCHI, R. KERMAN, AND L. PICK, *Boundary trace inequalities and rearrangements*, J. Anal. Math., 105 (2008), pp. 241–265, <https://doi.org/10.1007/s11854-008-0036-2>.
- [10] O. DAVYDOV, *Error bounds for a least squares meshless finite difference method on closed manifolds*, 2019, <https://arxiv.org/abs/1910.03359>.
- [11] N. FLYER, G. A. BARNETT, AND L. J. WICKER, *Enhancing finite differences with radial basis functions: experiments on the Navier-Stokes equations*, J. Comput. Phys., 316 (2016), pp. 39–62, <https://doi.org/10.1016/j.jcp.2016.02.078>.
- [12] N. FLYER, B. FORNBERG, V. BAYONA, AND G. A. BARNETT, *On the role of polynomials in RBF-FD approximations: I. Interpolation and accuracy*, J. Comput. Phys., 321 (2016), pp. 21–38, <https://doi.org/10.1016/j.jcp.2016.05.026>.
- [13] B. FORNBERG AND N. FLYER, *Fast generation of 2-D node distributions for mesh-free PDE discretizations*, Comput. Math. Appl., 69 (2015), pp. 531–544, <https://doi.org/10.1016/j.camwa.2015.01.009>.
- [14] B. FORNBERG, N. FLYER, AND J. M. RUSSELL, *Comparisons between pseudospectral and radial basis function derivative approximations*, IMA J. Numer. Anal., 30 (2010), pp. 149–172, <https://doi.org/10.1093/imanum/drn064>.
- [15] E. LARSSON, V. SHCHERBAKOV, AND A. HERYUDONO, *A least squares radial basis function partition of unity method for solving PDEs*, SIAM J. Sci. Comput., 39 (2017), pp. A2538–A2563, <https://doi.org/10.1137/17M1118087>.
- [16] G. R. LIU, B. B. T. KEE, AND L. CHUN, *A stabilized least-squares radial point collocation method (LS-RPCM) for adaptive analysis*, Comput. Methods Appl. Mech. Engrg., 195 (2006), pp. 4843–4861, <https://doi.org/10.1016/j.cma.2005.11.015>.
- [17] C. A. MICCHELLI, *Interpolation of scattered data: distance matrices and conditionally positive definite functions*, Constr. Approx., 2 (1986), pp. 11–22, <https://doi.org/10.1007/BF01893414>.
- [18] S. MILOVANOVIĆ AND L. VON SYDOW, *A high order method for pricing of financial derivatives using radial basis function generated finite differences*, 2018, <https://arxiv.org/abs/1808.05890>.
- [19] P.-O. PERSSON AND G. STRANG, *A simple mesh generator in Matlab*, SIAM Rev., 46 (2004), pp. 329–345, <https://doi.org/10.1137/S0036144503429121>, <https://doi.org/10.1137/S0036144503429121>.
- [20] A. PETRAS, L. LING, C. PIRET, AND S. J. RUUTH, *A least-squares implicit RBF-FD closest point method and applications to PDEs on moving surfaces*, J. Comput. Phys., 381 (2019), pp. 146–161, <https://doi.org/10.1016/j.jcp.2018.12.031>.
- [21] R. B. PLATTE AND T. A. DRISCOLL, *Eigenvalue stability of radial basis function discretizations for time-dependent problems*, Comput. Math. Appl., 51 (2006), pp. 1251–1268, <https://doi.org/10.1016/j.camwa.2006.04.007>.
- [22] R. SCHABACK, *All well-posed problems have uniformly stable and convergent discretizations*, Numer. Math., 132 (2016), pp. 597–630, <https://doi.org/10.1007/s00211-015-0731-8>.

- [23] I. J. SCHOENBERG, *Metric spaces and completely monotone functions*, Ann. of Math. (2), 39 (1938), pp. 811–841, <https://doi.org/10.2307/1968466>.
- [24] V. SHANKAR, *The overlapped radial basis function-finite difference (RBF-FD) method: a generalization of RBF-FD*, J. Comput. Phys., 342 (2017), pp. 211–228, <https://doi.org/10.1016/j.jcp.2017.04.037>.
- [25] V. SHANKAR, R. M. KIRBY, AND A. L. FOGELSON, *Robust node generation for mesh-free discretizations on irregular domains and surfaces*, SIAM J. Sci. Comp., 40 (2018), pp. A2584–A2608, <https://doi.org/10.1137/17M114090X>.
- [26] C. SHU, H. DING, AND K. YEO, *Local radial basis function-based differential quadrature method and its application to solve two-dimensional incompressible Navier–Stokes equations*, Comput. Methods Appl. Mech. Engrg., 192 (2003), pp. 941–954, [https://doi.org/10.1016/S0045-7825\(02\)00618-7](https://doi.org/10.1016/S0045-7825(02)00618-7).
- [27] J. SLAK AND G. KOSEC, *On generation of node distributions for meshless PDE discretizations*, SIAM J. Sci. Comp., 41 (2019), pp. A3202–A3229, <https://doi.org/10.1137/18M1231456>.
- [28] A. I. TOLSTYKH, *On using RBF-based differencing formulas for unstructured and mixed structured-unstructured grid calculations*, in Proceedings of the 16th IMACS World Congress on Scientific Computation, Applied Mathematics and Simulation, Lausanne, Switzerland, 2002.
- [29] K. VAN DER SANDE AND B. FORNBERG, *Fast variable density 3-D node generation*, 2019, <https://arxiv.org/abs/1906.00636>.
- [30] G. B. WRIGHT AND B. FORNBERG, *Scattered node compact finite difference-type formulas generated from radial basis functions*, J. Comput. Phys., 212 (2006), pp. 99–123, <https://doi.org/10.1016/j.jcp.2005.05.030>.